Device

Article

Trade-off between efficiency and stability in Mn^{2+}-doped perovskite light-emitting diodes

Graphical abstract

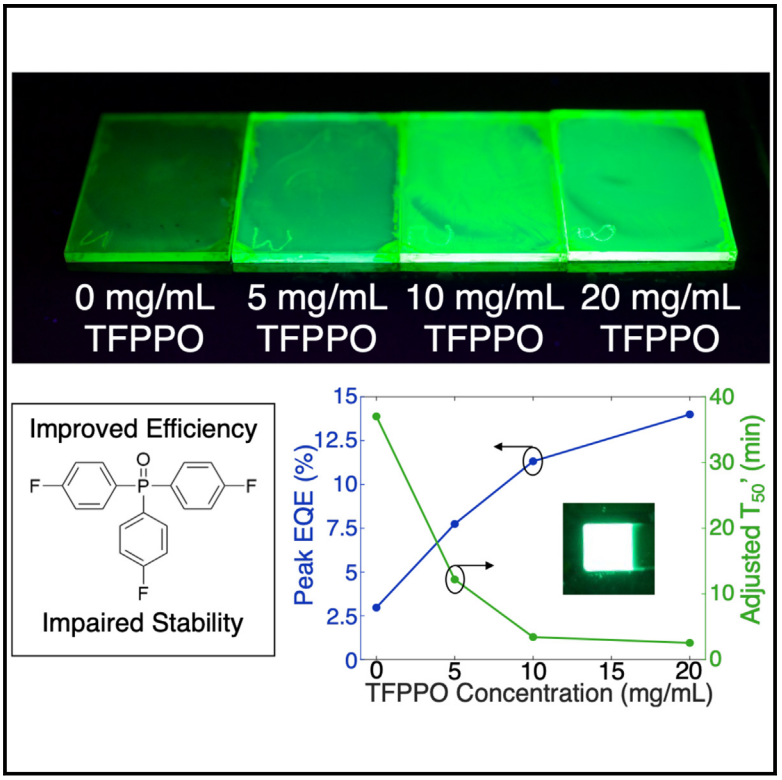

Highlights

- Analysis of the interplay between efficiency and stability in Mn^{2+}-doped PeLEDs
- Maximum luminance of 128,000 cd/m^2 achieved in a green Mn^{2+}-doped PeLED
- 14.0% external quantum efficiency achieved in a quasi-bulk 3D Mn^{2+}-doped PeLED
- Device-level electrical and photophysical characterization of Mn^{2+}-doped PeLEDs

Authors

Sebastian Fernández, William Michaels, Manchen Hu, ..., Junrui Lyu, Mahesh K. Gangishetty, Daniel N. Congreve

Correspondence

congreve@stanford.edu

In brief

This study presents a systematic analysis regarding the interplay between efficiency and stability in Mn^{2+}-doped perovskite light-emitting diodes (PeLEDs) with the introduction of tris(4-fluorophenyl)phosphine oxide (TFPPO) as a molecular additive. Increased levels of TFPPO treatment yield brighter thin films as well as enhanced device efficiencies (up to 14.0%). However, the stability of the Mn^{2+}-doped PeLEDs is impaired with higher TFPPO treatment (decreases from 37.0 to 2.54 min).

1 Understand
Early stage research on device properties, design, and physics

Fernández et al., 2023, Device *1*, 100017
August 25, 2023
https://doi.org/10.1016/j.device.2023.100017

CellPress

Device

CellPress
OPEN ACCESS

Article

Trade-off between efficiency and stability in Mn^{2+}-doped perovskite light-emitting diodes

Sebastian Fernández,[1] William Michaels,[1] Manchen Hu,[1] Pournima Narayanan,[1,2] Natalia Murrietta,[1] Arynn O. Gallegos,[1] Ghada H. Ahmed,[1] Junrui Lyu,[1] Mahesh K. Gangishetty,[3] and Daniel N. Congreve[1,4,*]

[1]Department of Electrical Engineering, Stanford University, Stanford, CA 94305, USA
[2]Department of Chemistry, Stanford University, Stanford, CA 94305, USA
[3]Department of Chemistry, Mississippi State University, Starkville, MS 39762, USA
[4]Lead contact
*Correspondence: congreve@stanford.edu
https://doi.org/10.1016/j.device.2023.100017

THE BIGGER PICTURE Perovskite light-emitting diodes (PeLEDs) are next-generation light-emission candidates given their fantastic properties, including sharp color purity, bandgap tunability, and inexpensive processing. This study explores the potential of Mn^{2+}-doped PeLEDs for lighting and display applications. By introducing a molecular additive, tris(4-fluorphenyl)phosphine oxide (TFPPO), Mn^{2+}-doped PeLEDs achieve a peak external quantum efficiency of 14.0% and peak luminance (i.e., brightness) of 128,000 cd/m^2. These high efficiencies and brightnesses suggest that Mn^{2+}-doped PeLEDs could be implemented in lighting or display applications. However, device stability is also important to consider. We find that introducing TFPPO compromises the stability of Mn^{2+}-doped PeLEDs—a decrease from 37.0 to 2.54 min. By analyzing both the optoelectronic and photophysical characteristics of Mn^{2+}-doped PeLEDs before and after device operation, we report insights into this efficiency-stability trade-off.

SUMMARY

Although perovskite light-emitting diodes (PeLEDs) have demonstrated external quantum efficiencies (EQEs) well over 20%, their instability limits their commercial viability. Incorporating transition-metal dopants has previously improved the brightness, stability, and efficiency of PeLEDs. Here, we dope Mn^{2+} ions into a quasi-bulk 3D perovskite and introduce tris(4-fluorophenyl)phosphine oxide (TFPPO) to achieve a 14.0% peak EQE and 128,000 cd/m^2 peak luminance. Whereas incorporating TFPPO into PeLEDs dramatically increases their EQE, it also severely compromises their stability. At a 5 mA/cm^2 electrical current bias, PeLEDs fabricated without TFPPO (2.97% EQE) and with TFPPO (14.0% EQE) decay to half their maximum luminance in 37.0 and 2.54 min, respectively. In order to investigate this trade-off in EQE and stability, we study both photophysical and optoelectronic characteristics before and after PeLED electrical operation. Although Mn^{2+}-doped PeLEDs hold the potential to enable bright and efficient lighting, device stability degradation mechanisms require further investigation.

INTRODUCTION

Metal halide perovskite semiconductors are promising candidates for next-generation optoelectronic devices such as solar cells,[1] lasers,[2] and light-emitting diodes.[3] This class of semiconductor is distinguished by its bandgap tunability, sharp color purity, high photoluminescence quantum yield (PLQY), high charge carrier mobilities, and inexpensive solution processing.[4] In 2014, one of the first perovskite light-emitting diodes (PeLEDs) was demonstrated with an external quantum efficiency (EQE) below 1%,[5] prompting further investigations to improve device efficiencies. The efficiency of PeLEDs has grown rapidly since then, resulting in EQEs exceeding 20% for green[6–8] and longer[9–11] wavelengths and 15% and 0.4% for blue[12] or shorter[13] wavelengths, respectively. Across all wavelength regimens, the rise in PeLED efficiency is driven by a substantial increase in material,[6,8,14] interface,[15,16] and device architecture optimizations.[17–19]

Metal halide perovskites have an ABX_3 structure, where A is an organic (e.g., methylammonium MA^+), inorganic (e.g., Cs^+), or hybrid (e.g., $Cs_{0.5}MA_{0.5}^+$) cation; B is typically Pb^{2+} or Sn^{2+}; and X is a halide anion (e.g., I^-, Br^-, Cl^-). Introducing B-site dopants into the metal halide perovskites' ABX_3 lattice has been shown to improve optoelectronic properties, resulting in higher EQE devices.[20–27] For instance, Liu et al.[22] doped Ni^{2+} ions into $CsPbI_3$

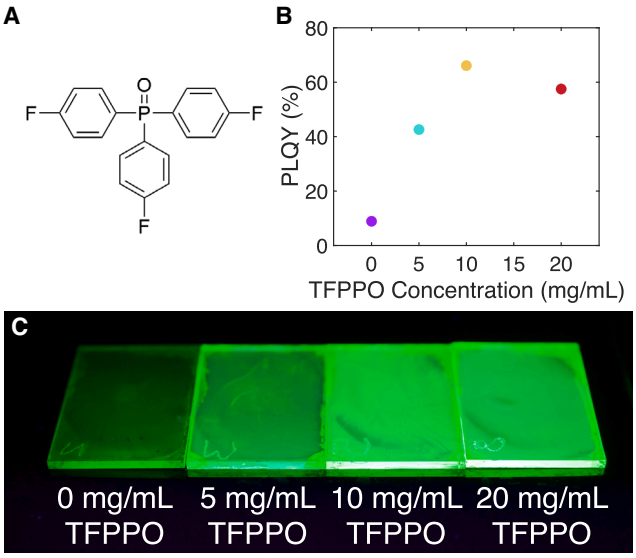

Figure 1. $(PEABr)_{0.2}Cs_{0.4}MA_{0.6}Pb_{0.7}Mn_{0.3}Br_3$ perovskites treated with TFPPO

(A) Chemical structure of the TFPPO additive.

(B) Photoluminescence quantum yield of Mn^{2+}-doped perovskites with increasing TFPPO-treated concentration.

(C) Photograph of perovskite films under 365 nm light in ambient air.

nanocrystals to achieve PLQYs exceeding 95% and improved material stability, leading to efficient red PeLEDs. In addition, we have previously investigated the effects of Mn^{2+} dopants on both perovskite nanocrystals[17,21,28] and thin films.[20,29] We found that Mn^{2+} dopants improve the brightness, EQE, and stability of PeLEDs based on quasi-bulk 2D/3D perovskites. These brightness, efficiency, and stability improvements can be explained by Mn^{2+} dopants enhancing the perovskite's PLQY, promoting uniform growth of the perovskite layer, and increasing the activation energy of ion migration, respectively.[20,29]

Recently, a new class of molecular additives has shown great promise to further improve PeLED efficiencies. Phosphine oxide additives, particularly triphenylphosphine oxide (TPPO) and its derivatives, have substantially improved PeLED efficiencies.[8,30] Within this molecular additive class, the P=O moiety coordinates with Pb^{2+} to reduce surface defect states.[31] As a result, nonradiative recombination pathways are diminished, leading to improved device EQE. For example, Xu et al.[30] fabricated TPPO-treated sky-blue PeLEDs with an emission peak at 488 nm and a maximum EQE of 9.5%. Tris(4-fluorophenyl)phosphine oxide (TFPPO), a fluorinated TPPO derivative, was incorporated into green PeLEDs by Ma et al.[8] Again, the P=O moiety served as a surface passivating agent to lower defect densities, yielding a 25.6% EQE green PeLED. Although there is significant evidence that TPPO additives and its derivatives largely serve to passivate surface defects via coordination with Pb^{2+}, the additives' effects on other cations (both in the A and B site) are not well understood and require further investigation before being universally adopted.[31]

B-site dopants and phosphine oxide additives have played a crucial role in enhancing PeLED efficiency. However, the operational stability of PeLEDs is ultimately the greatest obstacle limiting their commercial viability.[32] Although several potential explanations for limited PeLED stability have been identified, including joule heating,[19,33] interfacial reactions,[34,35] ion migration,[29,36–38] and charge injection imbalance,[39,40] the exact causes are still being investigated. Most efficiency-optimized green PeLEDs report operational lifetimes on the order of a few hours,[8,41–44] which is not competitive with mature organic[45] and III–V[46] light-emitting diode technologies. Careful consideration of both device efficiency and stability will be required to enable PeLED technologies for commercial applications.

In this work, we investigate the effects of TFPPO on Mn^{2+}-doped organic-inorganic hybrid quasi-bulk 3D $(PEABr)_{0.2}Cs_{0.4}MA_{0.6}Pb_{0.7}Mn_{0.3}Br_3$ thin films and its corresponding PeLED configuration. With optimized TFPPO treatment, we are able to boost the PLQY and efficiency of the Mn^{2+}-doped thin film and Mn^{2+}-doped PeLED, respectively. However, we find that the stability of the efficiency-optimized PeLEDs is significantly worse than PeLEDs without TFPPO treatment. To further uncover these effects, we measure repeated electrical scans and time-resolved photoluminescence (TRPL) spectra under identical electrical degradation conditions for all TFPPO-treated PeLEDs. We find that with higher TFPPO-treated concentrations, there is decreased robustness in operational luminance ($L_{oper.}$), maximum luminance (L_{max}), turn-on voltage (V_{on}), device resistance (R_{dev}), and average decay lifetime (τ_{avg}) under identical electrical degradation conditions. This work demonstrates the potential of bright, efficient, B-site-engineered PeLEDs for lighting and display applications while also providing insight into potential strategies for mitigating the detrimental effects of TFPPO on the stability of Mn^{2+}-doped PeLEDs.

RESULTS AND DISCUSSION

In this work, we replace 30% of the lead in all of our perovskite precursor solutions with manganese, resulting in organic-inorganic hybrid quasi-bulk 3D $(PEABr)_{0.2}Cs_{0.4}MA_{0.6}Pb_{0.7}Mn_{0.3}Br_3$ thin films. We introduce TFPPO (Figure 1A) to the thin films by dissolving it in the chloroform antisolvent, focusing primarily on 0, 5, 10, and 20 mg/mL TFPPO concentrations. We are able to synthesize TFPPO through the oxidation of tris(4-fluorophenyl)phosphine (TFPP) (Figure S1A) and confirm its structure by its ^{1}H-NMR spectrum (Figure S1B). Previously, we demonstrated a PLQY of 27% for $(PEABr)_{0.2}Cs_{0.4}MA_{0.6}Pb_{0.7}Mn_{0.3}Br_3$ thin films treated with a pure chloroform antisolvent.[20] Figure 1B shows a general increase in PLQY with increased TFPPO-treated concentrations achieving a maximum of 66% for the 10 mg/mL TFPPO concentration. We note that the 0 mg/mL PLQY of 8.9% is lower than previously reported[20] (27%) because we annealed the thin film as if it would be used in the PeLED configuration discussed later. In addition, Figure 1C shows all four TFPPO-treated perovskite thin films excited by 365 nm light. Lastly, AFM images from Figure S2 suggest that TFPPO treatment may alter the morphology of the Mn^{2+}-doped thin films.

Next, we incorporate the Mn^{2+}-doped thin films in a PeLED configuration given the general improvement in film brightness with TFPPO treatment. We employ a device architecture consisting of indium tin oxide (ITO; as the anode)/poly(3,4-ethylenedioxythiophene)polystyrene sulfonate (PEDOT:PSS) mixed with Nafion

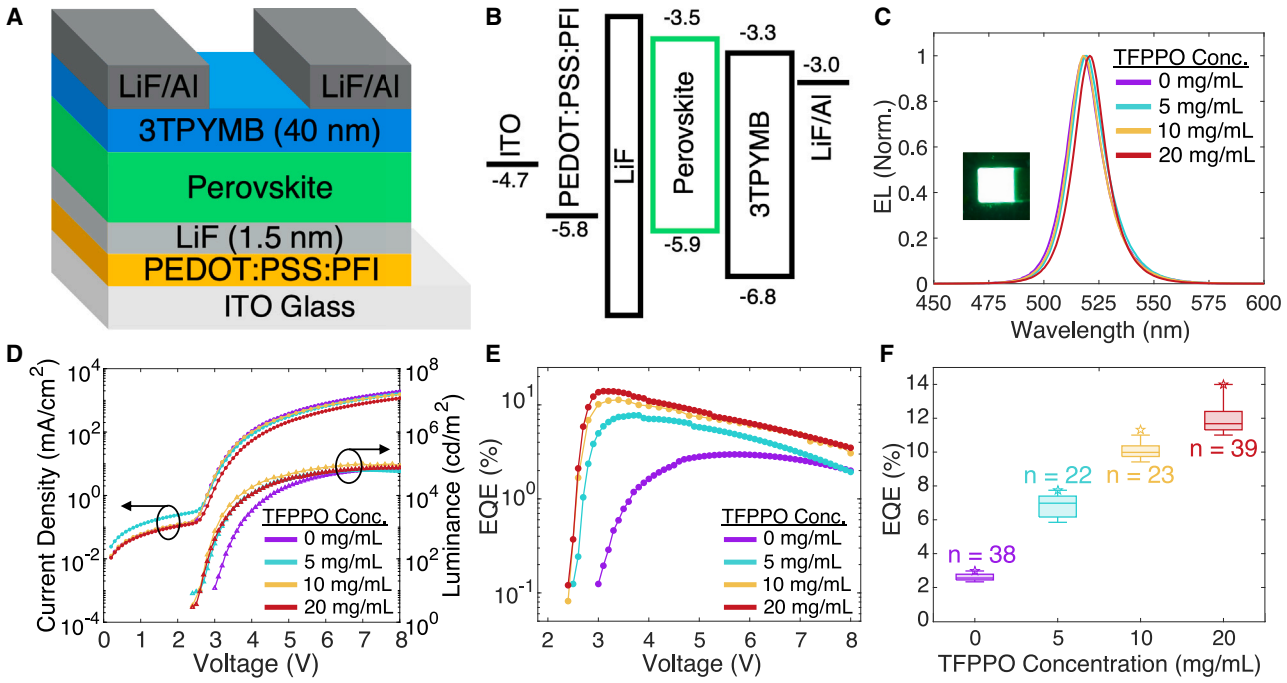

Figure 2. Green Mn^{2+}-doped perovskite LED performance

(A) Device structure schematic of TFPPO-treated $(PEABr)_{0.2}Cs_{0.4}MA_{0.6}Pb_{0.7}Mn_{0.3}Br_3$ PeLEDs.

(B) PeLED energy band diagram. The energy levels of the transport layers are from Ma et al.,[8] and the electrode work functions are from Gangishetty et al.[20] The energy levels of the perovskite layer were previously reported by Gangishetty et al.[20]

(C) Electroluminescence spectra of TFPPO-treated PeLEDs. Inset photograph shows a representative PeLED during operation.

(D and E) *J-V-L* (D) and EQE (E) characteristics of TFPPO-treated PeLEDs.

(F) Statistical distributions of maximum EQEs of TFPPO-treated PeLEDs. The number of devices in each distribution is annotated, and champion EQE devices are marked with a star.

perfluorinated ionomer (PEDOT:PSS:PFI, as the hole-transport layer)/lithium fluoride (LiF; as a 1.5 nm ultrathin underlayer)/$(PEABr)_{0.2}Cs_{0.4}MA_{0.6}Pb_{0.7}Mn_{0.3}Br_3$ (as the perovskite active layer)/tris[2,4,6-trimethyl-3-(pyridine-3-yl)phenyl]borane (3TPYMB; 40 nm of 3TPYMB, as the electron-transport layer)/lithium fluoride (LiF; as the electron-injection layer)/aluminum (Al, as the cathode). This structure is summarized in Figure 2A. We incorporate an ultrathin LiF underlayer to suppress photoluminescence quenching that occurs at the interface between the perovskite layer and adjacent transport layers,[18] reduce PeLED leakage current,[47] and improve the solution-based deposition of the perovskite layer by increasing its wettability.[16,47,48] In addition, the energy band diagram shown in Figure 2B shows the careful band alignment of both the electron-transport and hole-transport layers with the conduction and valence band edges of the perovskite, respectively. Figure 2C shows the electroluminescence of the four TFPPO-treated Mn^{2+}-doped PeLEDs with the inset depicting a representative TFPPO-treated PeLED with a device area of 4 mm^2. The EL peaks of the four devices lie between 518 and 521 nm. *J-V-L* and EQE characteristics are depicted for the champion efficiency devices at each TFPPO concentration in Figures 2D and 2E, respectively. Although the PLQY of the 0 mg/mL TFPPO-treated film is substantially lower than that of the 20 mg/mL TFPPO-treated film, the L_{max}s of the corresponding PeLEDs of 70,400 and 75,100 cd/m^2, respectively, are comparable, suggesting different charge injection efficiencies. The champion efficiency PeLEDs shown in Figure 2D achieve luminances as high as 98,800 cd/m^2. The champion brightness PeLEDs shown in Figure S3 achieve a L_{max} of 128,000 cd/m^2, which is among the highest luminances reported for PeLEDs.[6,33,49] In Figure 2E, the peak EQEs of the 0, 5, 10, and 20 mg/mL TFPPO-treated devices are 2.97%, 7.74%, 11.3%, and 14.0%, respectively, showing a nearly 5-fold enhancement from 0 to 20 mg/mL TFPPO treatment. In addition, Figure S4 shows all Mn^{2+}-doped PeLEDs achieve an EQE of over 1% for current densities of over 1,000 mA/cm^2, enabling high brightness irrespective of TFPPO treatment. We also study the *J-V-L* and EQE characteristics of 30 and 40 mg/mL TFPPO-treated PeLEDs as shown in Figures S5A and S5B. Because the 20 mg/mL TFPPO-treated PeLED demonstrates a peak EQE of 14.0% and the 30 and 40 mg/mL TFPPO-treated PeLEDs achieve peak EQEs of 11.6% and 10.7%, respectively, one can see that increased TFPPO treatment will not enhance device efficiencies any further. Finally, we demonstrate the reproducibility of the TFPPO-treated PeLEDs in Figure 2F through EQE device statistics across a total of 122 devices.

Now, we look toward characterizing the operational stability of these same Mn^{2+}-doped PeLEDs. In order to fairly compare[50] the operational lifetimes of the various TFPPO-treated PeLEDs, we define the following stability terms. The T_{50} metric (i.e., initial luminance half-lifetime) is defined as the time it takes the PeLED

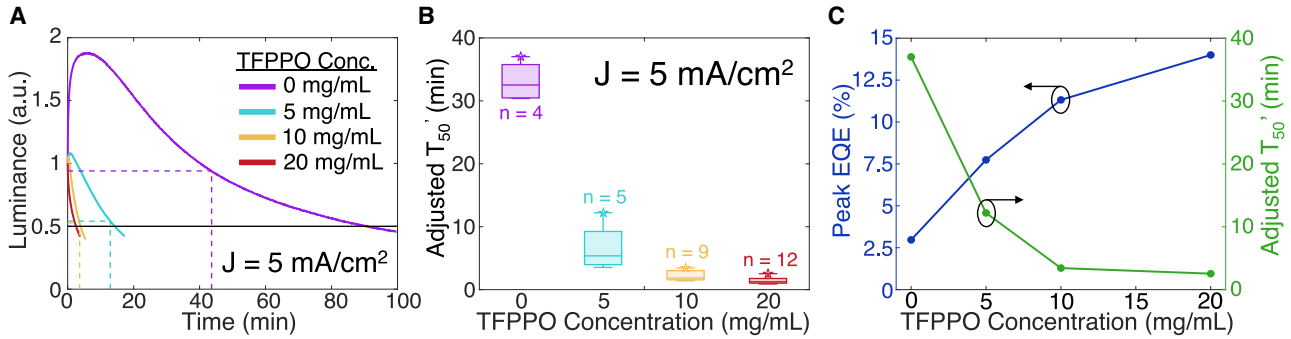

Figure 3. Operational stability of TFPPO-treated PeLEDs

(A) Luminance evolution in time of TFPPO-treated PeLEDs measured at an electrical current bias of 5 mA/cm^2. Each curve is normalized to its luminance at t = 0 s. Champion operational stability PeLEDs are shown. Dashed lines denote unadjusted maximum luminance half-lifetimes (unadjusted T_{50}'), whereas the intersections of the curves and the solid horizontal black line denote initial luminance half-lifetimes (T_{50}).

(B) Adjusted maximum luminance half-lifetime statistics of TFPPO-treated PeLEDs. The number of devices in each distribution is annotated, and champion operational stability devices are marked with a star.

(C) The trade-off between EQE and adjusted maximum luminance half-lifetimes across TFPPO-treated concentration. Champion operational stability devices at an electrical current bias of 5 mA/cm^2 are compared with champion EQE devices.

to degrade to half of its initial luminance. Because luminance overshoot, the phenomenon in which an LED's luminance may increase during operation, is prevalent in PeLED operation, we also consider a T_{50}' metric. The unadjusted T_{50}' time is defined as the time at which the PeLED has degraded to half of its L_{max}. The adjusted T_{50}' time (i.e., adjusted L_{max} half-lifetime) simply considers the time at which the PeLED reaches its L_{max} and sets this time to t = 0. We report both T_{50} and adjusted T_{50}' metrics for all TFPPO-treated PeLEDs but will primarily focus on adjusted T_{50}' times. In Figure 3A, the operational stability of TFPPO-treated PeLEDs is characterized at an electrical current bias of 5 mA/cm^2. The T_{50} times show a monotonic decrease with increasing TFPPO-treated concentration, with 0, 5, 10, and 20 mg/mL champion stability PeLEDs achieving T_{50} times of 90.7, 14.3, 3.93, and 2.54 min, respectively. Because the degree of luminance overshoot also decreases with increasing TFPPO-treated concentration, we focus on the adjusted T_{50}' times of 37.0, 12.2, 3.43, and 2.54 min for the 0, 5, 10, and 20 mg/mL TFPPO-treated champion stability devices, respectively. Figure S6 shows the corresponding electroluminescence spectra evolution in time that further illustrates how the adjusted T_{50}' times are extracted, as well as the strong spectral stability of all TFPPO-treated PeLEDs. Comparing the adjusted T_{50}' times of the 0 mg/mL (37.0 min) and 20 mg/mL TFPPO-treated PeLED (2.54 min), the EQE-optimized 20 mg/mL TFPPO-treated PeLED's champion stability is reduced by nearly a factor of 15. To ensure the reliability of our conclusions, we also report stability device statistics based on the adjusted T_{50}' times for all TFPPO-treated PeLEDs biased at 5 mA/cm^2 in Figure 3B, where one can see that across 30 PeLEDs there is a clear impairment of device stability with increased TFFPO-treated concentration. Furthermore, Figure S5C shows that higher TFPPO concentrations can further reduce PeLED operational stability, because both 30 and 40 mg/mL TFPPO-treated PeLEDs degrade to half of their L_{max} in less than 1 min of operation at an electrical current bias of 5 mA/cm^2. In Figure S7, we also characterize the operational stability of TFPPO-treated PeLEDs at a higher electrical current bias of 10 mA/cm^2. Both the luminance decay curves and stability device statistics reaffirm the trends observed at 5 mA/cm^2. Similarly, we also report the electroluminescence spectra evolution in time for the devices biased at 10 mA/cm^2 in Figure S8. Finally, we compare the adjusted T_{50}' times from the champion stability PeLEDs with the peak EQEs of the champion efficiency PeLEDs in Figure 3C to illustrate the trade-off between efficiency and stability in Mn^{2+}-doped PeLEDs. We summarize the device metrics associated with efficiency and stability of 0, 5, 10, and 20 mg/mL TFPPO-treated PeLEDs in Table 1.

To further investigate this trade-off between the peak EQE and adjusted T_{50}' time of TFPPO-treated Mn^{2+}-doped PeLEDs, we endeavor to uncover the evolution of PeLED optoelectronic properties with respect to cumulative electrical degradation. Previously, Warby et al.[51] studied a similar trade-off in efficiency and stability as it related to phenethylammonium bromide concentration within a $CsPbBr_3$ PeLED platform by analyzing *J-V-L* characteristics before and after electrical degradation.

We operate our TFPPO-treated PeLEDs at an electrical current bias of 10 mA/cm^2 for a total of 30 cumulative minutes. In Figures 4A–4D, we probe the optoelectronic properties of TFPPO-treated PeLEDs by measuring a *J-V-L* scan after 0, 2, 4, 8, and 16 min of operation (i.e., measured at t = 0, 2, 6, 14, and 30 min) for a total of five *J-V-L* scans corresponding to 30 min of cumulative electrical operation. With increasing TFPPO-treated concentration, we notice several PeLED optoelectronic properties degrade with device operation time, such as turn-on voltage (V_{on}, defined as the voltage when L = 1 cd/m^2), L_{max}, $L_{oper.}$ (L @ J = 10 mA/cm^2), and R_{dev} (@ ~ J = 10 mA/cm^2). In Figure 4E, ΔV_{on} (i.e., $V_{on} - V_{on,\ t\ =\ 0}$) is generally higher with increasing TFPPO-treated concentrations. This could imply that charge carrier injection worsens with increasing TFPPO-treated concentrations.[52] In particular, the 0 mg/mL TFPPO-treated PeLED's ΔV_{on} is much lower than the other three PeLEDs after 30 min of operation. Figure 4F shows that $L_{oper.}$ degrades more rapidly with higher concentrations of TFPPO and that after 30 min of operation, the 0 mg/mL TFPPO-treated device is more efficient (i.e., has a higher EQE) than

Table 1. Summarized device metrics of TFPPO-treated PeLEDs

Device metric	0 mg/mL TFPPO	5 mg/mL TFPPO	10 mg/mL TFPPO	20 mg/mL TFPPO
EL peak	519 nm	519 nm	518 nm	521 nm
FWHM	19 nm	19 nm	18 nm	17 nm
Maximum EQE	2.97%	7.74%	11.3%	14.0%
Maximum luminance	70,400 cd/m^2	62,800 cd/m^2	98,800 cd/m^2	75,100 cd/m^2
J = 10 mA/cm^2				
T_{50} lifetime	24.5 min	5.51 min	1.68 min	1.38 min
Adjusted (Adj.) T_{50}' lifetime	15.3 min	4.67 min	1.55 min	1.38 min
J = 5 mA/cm^2				
T_{50} lifetime	90.7 min	14.3 min	3.93 min	2.54 min
Adj. T_{50}' lifetime	37.0 min	12.2 min	3.43 min	2.54 min

Device metrics are from Figures 2, 3, and S7.

the 5 and 10 mg/mL TFPPO-treated devices. We note that Warby et al.[51] reported their trade-off between efficiency and stability based on the evolution of their PeLEDs' EQE, which we also see indirectly in Figure 4F. Moreover, we also consider the amount of light generated from the PeLEDs as they degrade to half of their maximum $L_{oper.}$ (i.e., unadjusted T_{50}' time). We calculate unadjusted T_{50}' times of 40.4, 5.1, 3.6, and 2.5 min for the 0, 5, 10, and 20 mg/mL TFPPO-treated PeLEDs, respectively, via linear extrapolation and interpolation of the $L_{oper.}$ curves in Figure 4F. We note that the unadjusted T_{50}' times of these PeLEDs achieve a higher value than that of their respective champion stability devices operated at J = 10 mA/cm^2 but are not included in the device stability statistics because of electrical scans being measured as the device is operated. Next, the amount of light generated from the PeLEDs is directly proportional to the integration of the $L_{oper.}$ curves from t = 0 to their respective unadjusted T_{50}' times. The integration yields values of 3,862, 2,150, 3,449, and 3,179 cd-min/m^2 for the 0, 5, 10, and 20 mg/mL TFPPO-treated PeLEDs, respectively. Thus, all four devices emit a similar amount of light as they decay to half of their maximum $L_{oper.}$ despite lower TFPPO-treated devices starting with a lower L_{max}. Next, in Figure S9A, we see that L_{max} also degrades more rapidly with increased TFPPO-treated concentrations, implying that lower TFPPO-treated PeLEDs are more robust for high-brightness applications. Figure S9B shows ΔR_{dev} (i.e., $R_{dev} - R_{dev,\ t\ =\ 0}$) with device operation time. All of the TFPPO-treated PeLEDs show a general increase in ΔR_{dev} except the 0 mg/mL PeLED, which has robust R_{dev}. After 30 min of operation, the 0 mg/mL PeLED also demonstrates an overall decrease in R_{dev}, which is not seen in the other TFPPO-treated PeLEDs. An increased R_{dev} can suggest either a decrease in charge mobility in the perovskite or charge transport layers or an increased barrier to injected charges originating from one or both contacts.

In addition, we also consider the amount of electrical energy introduced to the TFPPO-treated PeLEDs as they decay to half of their maximum $L_{oper.}$. The electrical power of these devices is derived using the R_{dev}s from Figure S9B and the operational current as shown in Figure S10. The 0 mg/mL TFPPO-treated PeLED does not decay to half of its L_{max} in Figure 4F within 30 min, but a lower bound of 0.802 mWh of electrical energy introduced as it decays is calculated. Next, the 5, 10, and 20 mg/mL TFPPO-treated PeLEDs all reach half of their maximum (i.e., initial) $L_{oper.}$ between 2 and 6 min of cumulative electrical operation as shown in Figure 4F. Similarly, an upper bound on the electrical energy introduced to these TFPPO-treated PeLEDs can be calculated by considering the energy supplied from t = 0 to t = 6 min. Using Figure S10, the upper bound of electrical energy introduced to the 5, 10, and 20 mg/mL TFPPO-treated PeLEDs as they decay to half of their maximum $L_{oper.}$ is 0.163, 0.149, and 0.164 mWh, respectively. Thus, the 0 mg/mL TFPPO-treated PeLED is introduced to, at minimum, approximately five times more electrical energy than the 5, 10, and 20 mg/mL TFPPO-treated devices as they decay to half of their maximum $L_{oper.}$. Furthermore, this implies that the 0 mg/mL TFPPO-treated PeLED is more stable than the 5, 10, and 20 mg/mL TFPPO-treated PeLEDs considering supplied electrical energy, which adds another dimension to the efficiency-stability trade-off.

Next, we aim to uncover a photophysical understanding of this efficiency-stability trade-off in Mn^{2+}-doped PeLEDs by conducting TRPL measurements. We initially measure both TRPL and PLQY characteristics of a pristine TFPPO-treated PeLED, followed by electrical operation for 1 h at J = 10 mA/cm^2, concluding with subsequent TRPL and PLQY measurements on the degraded device. Figure 5 shows the TRPL decay curves of all TFPPO-treated PeLEDs according to the aforementioned procedure. We then model the PL intensity with a biexponential model,[18,53,54] where A and B are amplitudes for each exponential and τ_1 and τ_2 are the extracted decay lifetimes:

$$I = A\exp(-t/\tau_1) + B\exp(-t/\tau_2). \quad \text{(Equation 1)}$$

τ_{avg} is an amplitude-weighted lifetime average defined as follows:

$$\tau_{avg} = (A/(A+B))\tau_1 + (B/(A+B))\tau_2. \quad \text{(Equation 2)}$$

Here, τ_1 is a fast decay related to trap-assisted nonradiative recombination at the grain boundaries within the perovskite, whereas τ_2 is a slow decay related to radiative recombination inside the grains of the perovskite.[18,55] Table 2 summarizes the τ_1, τ_2, and τ_{avg} for the four devices depicted in Figure 5 at a fluence of approximately 60 pJ/cm^2. For all PeLEDs treated with a nonzero concentration of TFPPO, the contribution of τ_1 (i.e., A/(A + B)) increases after electrical operation. Ma et al.[8] previously showed that the P=O moiety from TFPPO passivates the perovskite grain boundaries via coordination bonding with unsaturated sites. Thus, we hypothesize that a significant portion of the material degradation occurs at the perovskite grain boundaries in the 5, 10, and 20 mg/mL TFPPO-treated PeLEDs, but further studies are required. In general, the τ_{avg} of higher TFPPO-treated PeLEDs decreases more significantly with device operation. This is largely due to the impairment of τ_2's lifetime and overall contribution to τ_{avg}. For all PeLEDs except the 0 mg/mL TFPPO-treated device, the amplitude-weighted contribution from τ_2 decreases after 1 h of device operation. Figure S11 shows the time-resolved PL spectra, which further illustrates this larger suppression of the delayed fluorescence with higher TFPPO-treated concentration. Although the decay curves are

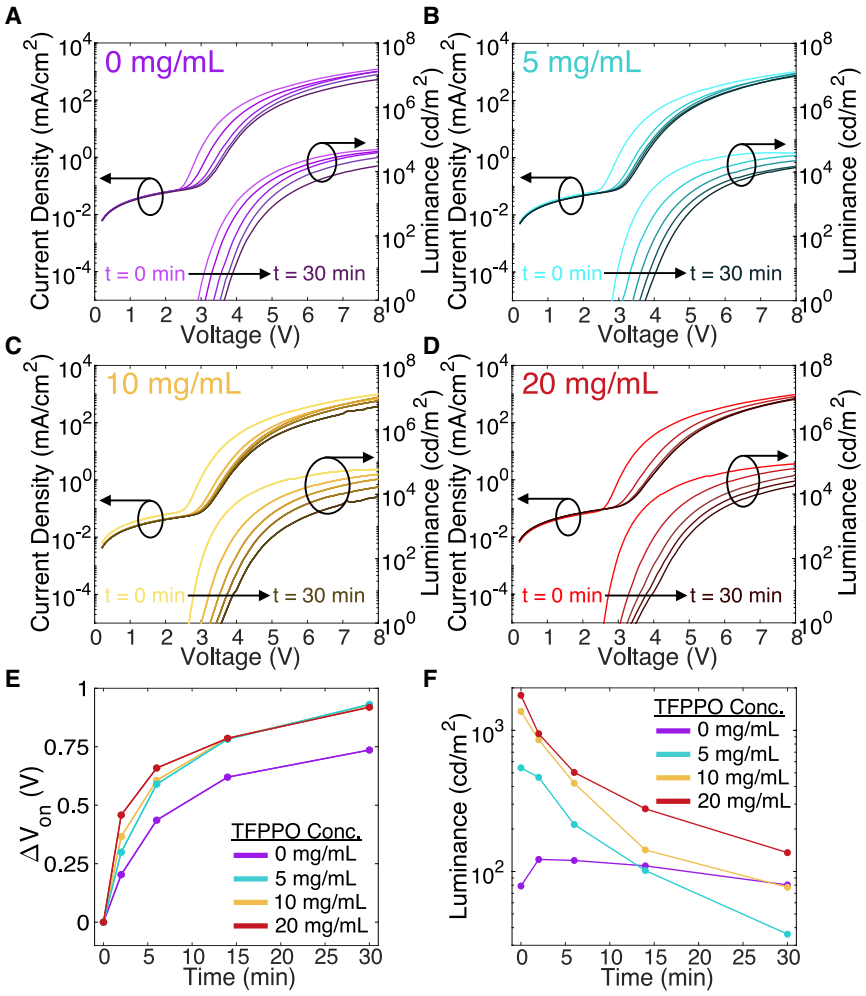

Figure 4. Optoelectronic parameter evolution of TFPPO-treated PeLEDs characterized via repeated electrical scans

(A–D) Repeated *J-V-L* scans of (A) 0, (B) 5, (C) 10, and (D) 20 mg/mL TFPPO-treated PeLEDs. A *J-V-L* measurement was taken for all PeLEDs after 2, 4, 8, and 16 min of operation at an electrical current bias of 10 mA/cm^2 for a total of 30 min of electrical degradation.

(E and F) Change in turn-on voltage (E) and operational luminance (J = 10 mA/cm^2) (F) of all TFPPO-treated PeLEDs as a function of cumulative electrical degradation time.

modeled well in Figure 5D, Figure S11G shows that a portion of the delayed fluorescence is not captured for the 20 mg/mL TFPPO-treated device. Thus, we also measure the TRPL of a 20 mg/mL TFPPO-treated PeLED using a lower repetition rate in Figure S12 with extracted lifetime parameters summarized in Table S1. At this lower repetition rate, we still see a substantial impairment of τ_{avg} with device operation. In order to ensure that these dynamics are not fluence dependent, we repeat the experiment at a higher fluence as shown in Figure S13 and summarized in Table S2. We can see that τ_{avg}'s evolution follows the same general trend as in Figure 5.

Finally, we study the evolution of the PLQY of TFPPO-treated PeLEDs both before and after 1 h of electrical operation at J = 10 mA/cm^2. The PLQY of the 10 mg/mL TFPPO-treated PeLED decreases after electrical operation, whereas both the τ_1 and τ_2 lifetimes increase. This can be explained by both the larger increase and decrease in the amplitude-weighted factors associated with the τ_1 and τ_2 lifetimes, respectively, as compared with the other TFPPO-treated PeLEDs. Thus, the 10 mg/mL TFPPO-treated PeLED's recombination dynamics are more dominated by nonradiative recombination processes after electrical operation compared with the other TFPPO-treated PeLEDs, which explain the decrease in PLQY despite increased τ_1 and τ_2 lifetimes. Table 2 shows that the ratio of the degraded PeLED's PLQY to the pristine PeLED's PLQY monotonically decreases with TFPPO concentration. Because the PLQY is the ratio of the radiative recombination rate to the sum of both radiative and nonradiative recombination rates and given the decrease in τ_{avg} after operation, we conclude that the nonradiative recombination pathways within higher TFPPO-treated PeLEDs are enhanced to a larger extent as compared with PeLEDs with lower TFPPO treatment under identical electrical operating conditions. This result paired with the analysis of the TRPL decay curves supports the following combined conclusion: the enhanced emissive efficiency induced by increased TFPPO treatment is more severely impaired as compared with decreased TFPPO treatment in Mn^{2+}-doped PeLEDs under identical electrical operating conditions. Furthermore, this explains why the higher TFPPO-treated PeLEDs initially perform better, as shown in Figure 2, but these performance gains are not resilient under identical operating conditions, as shown primarily in Figures 3 and 4.

Conclusions

In this work, we have systematically studied the effects of TFPPO on Mn^{2+}-doped PeLEDs' efficiency and stability. Although TFPPO can increase the PeLED's EQE by nearly 5-fold, its operational stability is degraded by nearly 15-fold. In general, under identical electrical degradation conditions, the optoelectronic properties (i.e., V_{on}, $L_{oper.}$, L_{max}, and R_{dev}) of higher TFPPO-treated PeLEDs degrade to a larger extent as compared with lower TFPPO-treated PeLEDs. In addition, TRPL characteristics show that the slower lifetime associated with radiative recombination in TFPPO-treated PeLEDs is substantially suppressed with identical electrical operating conditions, which in turn forfeits efficiency-boosting properties from the TFPPO treatment. These results simultaneously illustrate the potential of efficient B-site doped metal halide perovskites for light emission (see Table S3) while also suggesting that

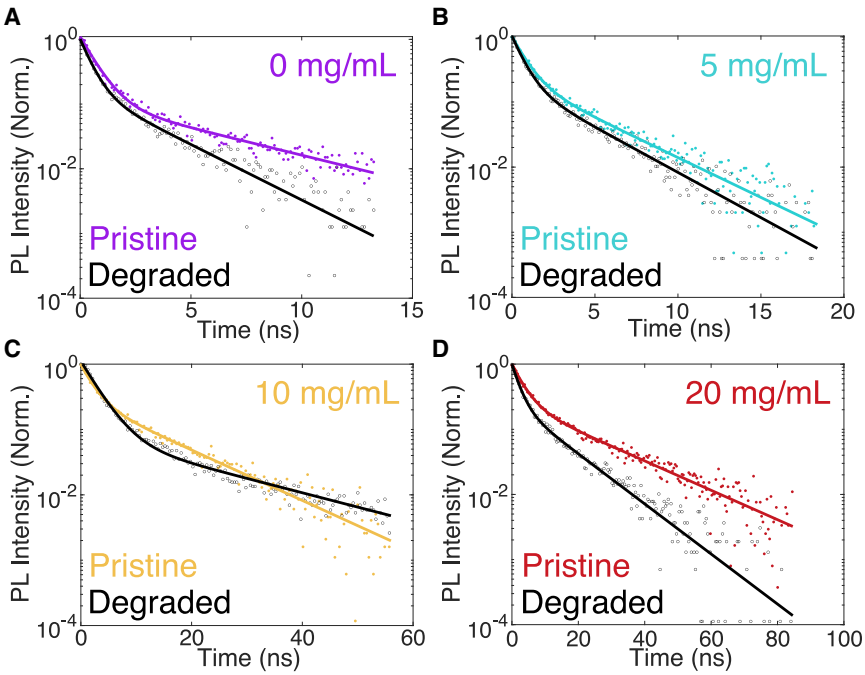

Figure 5. Photophysical characterization before and after device operation of TFPPO-treated PeLEDs

(A–D) Time-resolved photoluminescence decay curves of (A) 0, (B) 5, (C) 10, and (D) 20 mg/mL TFPPO-treated PeLEDs both prior to (pristine device) and after (degraded device) 1 h of electrical operation at 10 mA/cm^2. Note the difference in the time-axis scales.

further investigations are needed to mitigate stability degradation mechanisms induced by TFPPO treatment.

EXPERIMENTAL PROCEDURES

Resource availability

Lead contact

Further information and requests for resources and materials should be directed to and will be fulfilled by the lead contact, Daniel N. Congreve (congreve@stanford.edu).

Materials availability

All commercially available starting reagents and solvents were used directly without further treatment unless otherwise specified.

Data and code availability

The published article includes all data analyzed in this study. Data are available from the lead contact upon reasonable request.

Materials

Phenethylammonium bromide (PEABr) was purchased from Greatcell Solar Materials. Cesium bromide (CsBr; 99.999%), lead(II) bromide ($PbBr_2$, ultra dry, 99.999%), and anhydrous chloroform ($CHCl_3$; extra dry, 99.9%) were purchased from Thermo Fisher Scientific. Methylammonium bromide (MABr; ≥99%), manganese(II) bromide ($MnBr_2$, 98%), TFPP (98%), hydrogen peroxide (30%, stabilized), anhydrous dimethyl sulfoxide (DMSO; ≥99.9%), anhydrous *N,N*-dimethylformamide (DMF; 99.8%), Nafion perfluorinated resin solution (1,100 W, 5 wt % in lower aliphatic alcohols and water, contains 15–20% water), and LiF (≥99.99%) were purchased from Sigma-Aldrich. Magnesium sulfate ($MgSO_4$) and sodium chloride (NaCl) were purchased from Fisher Scientific Company. PEDOT:PSS (Clevios AI 4083) was purchased from Heraeus. 3TPYMB (>99%, sublimed) was purchased from Luminescence Technology Corporation. Al (99.99%) pellets were purchased from Kurt J. Lesker Company. All chemicals were used directly as received.

Perovskite precursors

The following preparation was conducted inside a nitrogen-filled glovebox at room temperature. 0.3 M stock solutions of PEABr, MABr, $PbBr_2$, and $MnBr_2$ were prepared by individually dissolving 0.6 mmol of each bromide precursor in 2 mL of DMF and left stirring for 1 h before synthesizing the final perovskite composition. Similarly, 0.6 mmol $CsPbBr_3$ was dissolved in 2 mL DMSO and stirred for 2 h before synthesizing the final perovskite composition. These five precursor solutions were then mixed in appropriate ratios to yield $(PEABr)_{0.2}Cs_{0.4}MA_{0.6}Pb_{0.7}Mn_{0.3}Br_3$, where a total of 20% of PEABr was added with respect to the A site. This final perovskite solution was then filtered with a 0.45 μm PTFE syringe filter immediately before spin coating.

TFPPO synthesis and NMR characterization

The following reaction (Figure S1A) was performed under nitrogen atmosphere according to the protocol reported by Ma et al.[8] A total of 2.00 g of TFPP (6.3 mmol) was dissolved in 10 mL of $CHCl_3$. Upon complete dissolution, 10 mL of 30% hydrogen peroxide was added dropwise to the reaction flask over 2 min. The reaction was vigorously stirred overnight at room temperature. The resulting crude was extracted with another 15 mL of $CHCl_3$. The chloroform layer was washed twice with brine solution. The chloroform layer was dried using $MgSO_4$, and the resulting solution was gravity filtered. The solution was dried overnight at 70°C. The yield was ~40%, and the resulting white powder was confirmed to be TFPPO using ^{1}H-NMR in d_6-DMSO solvent. One-dimensional ^{1}H-NMR analysis (Figure S1B) was performed at room temperature using a Brucker *Neo* 500 MHz NMR spectrometer. ^{1}H-NMR (500 MHz, DMSO-d_6) δ = 7.68 ppm (m, 6H) and 7.41 ppm (ddt, J = 8.9 Hz, 6.6 Hz, 2.1 Hz, 6H).

Device fabrication

ITO patterned glass substrates (100-nm ITO thickness; 20 Ω/square ITO resistance, Ossila 20 × 15 mm ITO Glass Substrates) were cleaned sequentially via sonication in deionized water, acetone, and isopropanol for 5 min per solvent. These substrates were then dried under compressed air and transferred to a Jelight UV-Ozone Cleaner to be further treated with O_2 plasma for 15 min immediately before PEDOT:PSS:PFI spin coating. The mixed PEDOT:PSS:PFI solution was synthesized by mixing 1.0 mL of 0.2 μm PVDF syringe-filtered PEDOT:PSS and 1.2 mL of Nafion perfluorinated resin solution and stirring at room temperature for 4 h prior to spin coating. ITO patterned glass substrates and the PEDOT:PSS:PFI stirred solution were then transferred to a nitrogen-filled glovebox where 200 μL of PEDOT:PSS:PFI was statically dispensed on the substrate. PEDOT:PSS:PFI was then spin-coated at 500 rpm for 5 s, followed by a 1,000 rpm/s ramp, and a final 4,500 rpm step for 90 s. Next, all ITO/PEDOT:PSS:PFI substrates were annealed together at 150°C for 20 min. Samples were then stored overnight to purge the nitrogen-filled glovebox of any residual moisture from PEDOT:PSS:PFI spin coating. Next, the substrates were transferred to a high-vacuum thermal evaporation chamber housed within a nitrogen-filled glovebox where 1.5 nm of LiF was deposited at a rate of 0.07 Å/s at a pressure of 8 × 10^{-6} mbar. Then, 40 mg of TFPPO was dissolved in 2 mL of $CHCl_3$ and stirred for 10 min to synthesize a 20 mg/mL TFPPO stock solution. Stock solutions of 5 and 10 mg/mL TFPPO were synthesized by serial dilution of the 20 mg/mL TFPPO solution. Similarly, 30 and 40 mg/mL TFPPO stock solutions were derived from a 40 mg/mL TFPPO stock solution and $CHCl_3$. Next, 150 μL of the aforementioned final perovskite solution was statically dispensed on the substrate and then spin-coated at 1,000 rpm for 10 s, followed

Table 2. Extracted time-resolved PL parameters and PLQY evolution of TFPPO-treated PeLEDs before and after 1 h of electrical operation at 10 mA/cm^2

TFPPO concentration	τ_1 (A/(A + B))	τ_2 (B/(A + B))	τ_{avg}	r^2	Fluence	$\frac{PLQY_{Degraded}}{PLQY_{Pristine}}$
0 mg/mL					57.3 pJ/cm^2	0.833
Pristine	0.667 ns (89.8%)	5.15 ns (10.2%)	1.12 ns	0.9893		
Degraded	0.478 ns (83.1%)	2.53 ns (16.9%)	0.825 ns	0.9973		
5 mg/mL					57.3 pJ/cm^2	0.674
Pristine	0.774 ns (77.0%)	3.55 ns (23.0%)	1.41 ns	0.9972		
Degraded	0.649 ns (80.3%)	3.13 ns (19.7%)	1.14 ns	0.9969		
10 mg/mL					60.2 pJ/cm^2	0.574
Pristine	2.13 ns (70.9%)	11.3 ns (29.1%)	4.80 ns	0.9976		
Degraded	2.94 ns (92.7%)	19.8 ns (7.3%)	4.17 ns	0.9913		
20 mg/mL					60.2 pJ/cm^2	0.357
Pristine	3.42 ns (73.7%)	19.2 ns (26.3%)	7.57 ns	0.9966		
Degraded	2.20 ns (75.4%)	11.3 ns (24.6%)	4.44 ns	0.9983		

Extracted time-resolved PL parameters are from Figure 5.

by a 600 rpm/s ramp and a final 2,800 rpm step for 45 s. At 30 s after the beginning of this spin-coating deposition, 90 μL of the chloroform antisolvent (0 mg/mL TFPPO, 5 mg/mL TFPPO, 10 mg/mL TFPPO, 20 mg/mL TFPPO, 30 mg/mL TFPPO, or 40 mg/mL TFPPO) was quickly dripped onto the substrates. The authors highly suggest replacing the foil in the spin-coater bowl after every processed substrate because we found this crucial for the fabrication of reproducible devices. The perovskite film thicknesses were measured to be 84.5 ± 9.97 nm across all TFPPO-treated concentrations. Then, all the ITO/PEDOT:PSS:PFI/LiF/$(PEABr)_{0.2}Cs_{0.4}MA_{0.6}Pb_{0.7}Mn_{0.3}Br_3$ samples were annealed together at 80°C for 10 min to remove any residual solvents. After the substrates cooled down to room temperature, they were then transferred to a high-vacuum thermal evaporation chamber housed within a nitrogen-filled glovebox where 40 nm of 3TPYMB, 1 nm of LiF, and 60 nm of Al were sequentially deposited at a rate of 2.5, 0.05, and 3 Å/s, respectively, at a pressure of 8×10^{-6} mbar.

Device characterization

Fully fabricated devices were encapsulated using a coverslip (Ossila) and ultraviolet epoxy (EPO-TEK OG159-2) before device measurements. Electroluminescence spectra were captured using an Ocean Insight QE Pro with 400 μA sourced to the device from a Keithley 2400. Operational stability curves were gathered using the same setup by sourcing either 400 μA (10 mA/cm^2) or 200 μA (5 mA/cm^2) of constant current and measuring the electroluminescence every 6 s of device operation. *J-V-L* characteristics were captured using an HP4145A and a calibrated Thorlabs photodiode (FDS1010-CAL) mounted just above the face of the device. The device (2 mm × 2 mm) is much smaller than the photodiode, which is smaller than the ITO patterned glass substrate. The photodiode is housed within a black 3D printed holder in order to prevent the collection of wave-guided light. Together, these two conditions ensure that EQE characteristics are not overestimated.[20,56]

Repeated *J-V-L* scans shown in Figures 4A–4D were captured using the same protocol listed above. In addition, an electrical current bias of 10 mA/cm^2 and 30 min of cumulative operation time was chosen based on the luminance lifetimes at 10 mA/cm^2 of the TFPPO-treated PeLEDs shown in Table 1, where all four devices achieve T_{50} and adjusted T_{50}' times less than 30 min. Also, because the shortest lifetime we reported at this electrical operating condition is 1.38 min, we designed our experiment such that we measured the first successive *J-V-L* scan after 2 min of operation. We also opted for a logarithmic spacing in operation time between *J-V-L* scans because the luminance decays of our PeLEDs followed a quasi-exponential decay (Figure S7A).

Structural and optical characterizations

AFM measurements were gathered in ambient air using a Bruker Dimension Icon ScanAsyst with PeakForce mode. The PLQY of both the perovskite films and fully fabricated devices were measured in an integrating sphere (Labsphere) excited by a 405 nm laser (MDL-III-405-100 mW; HJ Optronics) following de Mello et al.[57] The integrating sphere and spectrometer (QE Pro; Ocean Insight) were calibrated using a radiometric calibration source (HL-3P-INT-CAL; Ocean Insight). Perovskite films were unencapsulated, whereas fully fabricated devices were encapsulated. In addition, all components were calibrated against a calibrated Newport photodetector.[20] Time-resolved PL measurements were captured on fully fabricated devices as a function of time on a Hamamatsu C10627 streak unit coupled with a SP2150i spectrograph and C9300 digital camera. The excitation source was a Hamamatsu pulsed 379 nm laser with a 20 MHz repetition rate (0 and 5 mg/mL TFPPO-treated devices), 5 MHz repetition rate (10 and 20 mg/mL TFPPO-treated devices), or 2 MHz (Figure S12) repetition rate. In order to ensure proper modeling of the extracted lifetimes,[58] particularly the fast τ_1 lifetime, we also report the instrument response functions (IRFs) for all repetition rates used in Figure S14. We saw that all reported lifetimes are larger than the IRF lifetime at any given repetition rate. This also explains why both 5 and 2 MHz repetition rates were needed for the 20 mg/mL TFPPO-treated PeLED.

SUPPLEMENTAL INFORMATION

Supplemental information can be found online at https://doi.org/10.1016/j.device.2023.100017.

ACKNOWLEDGMENTS

S.F. was supported by Stanford University as a Diversifying Academia, Recruiting Excellence (DARE) Fellow; the U.S. Department of Energy (DOE) Building Technologies Office (BTO) as an IBUILD Graduate Research Fellow; Stanford Graduate Fellowship in Science & Engineering (SGF) as a P. Michael Farmwald Fellow; and the National GEM Consortium as a GEM Fellow. M.H. was supported by the Department of Electrical Engineering at Stanford University. P.N. was supported by an SGF as a Gabilan Fellow. A.O.G. was supported by a National Science Foundation Graduate Research Fellowship under grant DGE-1656518 and an SGF as a Scott A. and Geraldine D. Macomber Fellow. A portion of this work was performed at the Stanford Nano Shared Facilities (SNSF), supported by the National Science Foundation under award ECCS-2026822. This research was performed under an appointment to the Building Technologies Office (BTO) IBUILD Graduate Research Fellowship administered by the Oak Ridge Institute for Science and Education (ORISE) and managed by Oak Ridge National Laboratory (ORNL) for the DOE. ORISE is managed by Oak Ridge Associated Universities (ORAU). All opinions expressed in this paper are the authors' and do not necessarily reflect the policies and views of the DOE, EERE, BTO, ORISE, ORAU, or ORNL.

AUTHOR CONTRIBUTIONS

S.F. designed and performed experiments, analyzed data, and wrote the manuscript. S.F., W.M., M.H., and J.L. performed EQE measurements. S.F., W.M., and M.H. performed device stability measurements. S.F. and W.M. fabricated all devices. W.M. performed repeated current-voltage-luminance measurements. M.H. performed AFM measurements. P.N. synthesized and purified TFPPO. S.F., W.M., P.N., N.M., and A.O.G. performed PLQY and TRPL characterization measurements. G.H.A. and M.G. provided data analysis. D.N.C. supervised the research. All of the authors discussed the results and contributed to the manuscript.

DECLARATION OF INTERESTS

The authors declare no competing interests.

INCLUSION AND DIVERSITY

We support inclusive, diverse, and equitable conduct of research.

Received: April 26, 2023
Revised: June 9, 2023
Accepted: July 6, 2023
Published: August 1, 2023

REFERENCES

1. Green, M.A., Ho-Baillie, A., and Snaith, H.J. (2014). The Emergence of Perovskite Solar Cells. Nat. Photonics *8*, 506–514. https://doi.org/10.1038/nphoton.2014.134.
2. Zhang, Q., Shang, Q., Su, R., Do, T.T.H., and Xiong, Q. (2021). Halide Perovskite Semiconductor Lasers: Materials, Cavity Design, and Low Threshold. Nano Lett. *21*, 1903–1914. https://doi.org/10.1021/acs.nanolett.0c03593.
3. Fakharuddin, A., Gangishetty, M.K., Abdi-Jalebi, M., Chin, S.-H., bin Mohd Yusoff, A.R., Congreve, D.N., Tress, W., Deschler, F., Vasilopoulou, M., and Bolink, H.J. (2022). Perovskite Light-Emitting Diodes. Nat. Electron. *5*, 203–216. https://doi.org/10.1038/s41928-022-00745-7.
4. Chouhan, L., Ghimire, S., Subrahmanyam, C., Miyasaka, T., and Biju, V. (2020). Optoelectronic Properties and Applications of Halide Perovskites. Chem. Soc. Rev. *49*, 2869–2885. https://doi.org/10.1039/C9CS00848A.
5. Tan, Z.-K., Moghaddam, R.S., Lai, M.L., Docampo, P., Higler, R., Deschler, F., Price, M., Sadhanala, A., Pazos, L.M., Credgington, D., et al. (2014). Bright Light-Emitting Diodes Based on Organometal Halide Perovskite. Nat. Nanotechnol. *9*, 687–692. https://doi.org/10.1038/nnano.2014.149.
6. Kim, J.S., Heo, J.-M., Park, G.-S., Woo, S.-J., Cho, C., Yun, H.J., Kim, D.-H., Park, J., Lee, S.-C., Park, S.-H., et al. (2022). Ultra-Bright, Efficient and Stable Perovskite Light-Emitting Diodes. Nature *611*, 688–694. https://doi.org/10.1038/s41586-022-05304-w.
7. Lin, K., Xing, J., Quan, L.N., de Arquer, F.P.G., Gong, X., Lu, J., Xie, L., Zhao, W., Zhang, D., Yan, C., et al. (2018). Perovskite Light-Emitting Diodes with External Quantum Efficiency Exceeding 20 per Cent. Nature *562*, 245–248. https://doi.org/10.1038/s41586-018-0575-3.
8. Ma, D., Lin, K., Dong, Y., Choubisa, H., Proppe, A.H., Wu, D., Wang, Y.-K., Chen, B., Li, P., Fan, J.Z., et al. (2021). Distribution Control Enables Efficient Reduced-Dimensional Perovskite LEDs. Nature *599*, 594–598. https://doi.org/10.1038/s41586-021-03997-z.
9. Xie, M., Guo, J., Zhang, X., Bi, C., Zhang, L., Chu, Z., Zheng, W., You, J., and Tian, J. (2022). High-Efficiency Pure-Red Perovskite Quantum-Dot Light-Emitting Diodes. Nano Lett. *22*, 8266–8273. https://doi.org/10.1021/acs.nanolett.2c03062.
10. Liu, Y., Tao, C., Cao, Y., Chen, L., Wang, S., Li, P., Wang, C., Liu, C., Ye, F., Hu, S., et al. (2022). Synergistic Passivation and Stepped-Dimensional Perovskite Analogs Enable High-Efficiency near-Infrared Light-Emitting Diodes. Nat. Commun. *13*, 7425. https://doi.org/10.1038/s41467-022-35218-0.
11. Guo, B., Lai, R., Jiang, S., Zhou, L., Ren, Z., Lian, Y., Li, P., Cao, X., Xing, S., Wang, Y., et al. (2022). Ultrastable Near-Infrared Perovskite Light-Emitting Diodes. Nat. Photonics *16*, 637–643. https://doi.org/10.1038/s41566-022-01046-3.
12. Jiang, Y., Sun, C., Xu, J., Li, S., Cui, M., Fu, X., Liu, Y., Liu, Y., Wan, H., Wei, K., et al. (2022). Synthesis-on-Substrate of Quantum Dot Solids. Nature *612*, 679–684. https://doi.org/10.1038/s41586-022-05486-3.
13. Hu, M., Fernández, S., Zhou, Q., Narayanan, P., Saini, B., Schloemer, T.H., Lyu, J., Gallegos, A.O., Ahmed, G.H., and Congreve, D.N. (2023). Water Additives Improve the Efficiency of Violet Perovskite Light-Emitting Diodes. Matter *6*, 1–12. https://doi.org/10.1016/j.matt.2023.05.018.
14. Liu, Z., Qiu, W., Peng, X., Sun, G., Liu, X., Liu, D., Li, Z., He, F., Shen, C., Gu, Q., et al. (2021). Perovskite Light-Emitting Diodes with EQE Exceeding 28% through a Synergetic Dual-Additive Strategy for Defect Passivation and Nanostructure Regulation. Adv. Mater. *33*, 2103268. https://doi.org/10.1002/adma.202103268.
15. Tang, L., Qiu, J., Wei, Q., Gu, H., Du, B., Du, H., Hui, W., Xia, Y., Chen, Y., and Huang, W. (2019). Enhanced Performance of Perovskite Light-Emitting Diodes via Diamine Interface Modification. ACS Appl. Mater. Interfaces *11*, 29132–29138. https://doi.org/10.1021/acsami.9b11866.
16. Zhao, B., Lian, Y., Cui, L., Divitini, G., Kusch, G., Ruggeri, E., Auras, F., Li, W., Yang, D., Zhu, B., et al. (2020). Efficient Light-Emitting Diodes from Mixed-Dimensional Perovskites on a Fluoride Interface. Nat. Electron. *3*, 704–710. https://doi.org/10.1038/s41928-020-00487-4.
17. Gangishetty, M.K., Hou, S., Quan, Q., and Congreve, D.N. (2018). Reducing Architecture Limitations for Efficient Blue Perovskite Light-Emitting Diodes. Adv. Mater. *30*, 1706226. https://doi.org/10.1002/adma.201706226.
18. Shi, Y., Wu, W., Dong, H., Li, G., Xi, K., Divitini, G., Ran, C., Yuan, F., Zhang, M., Jiao, B., et al. (2018). A Strategy for Architecture Design of Crystalline Perovskite Light-Emitting Diodes with High Performance. Adv. Mater. *30*, 1800251. https://doi.org/10.1002/adma.201800251.
19. Zhao, L., Roh, K., Kacmoli, S., Al Kurdi, K., Jhulki, S., Barlow, S., Marder, S.R., Gmachl, C., and Rand, B.P. (2020). Thermal Management Enables Bright and Stable Perovskite Light-Emitting Diodes. Adv. Mater. *32*, 2000752. https://doi.org/10.1002/adma.202000752.
20. Gangishetty, M.K., Sanders, S.N., and Congreve, D.N. (2019). Mn2+ Doping Enhances the Brightness, Efficiency, and Stability of Bulk Perovskite Light-Emitting Diodes. ACS Photonics *6*, 1111–1117. https://doi.org/10.1021/acsphotonics.9b00142.
21. Hou, S., Gangishetty, M.K., Quan, Q., and Congreve, D.N. (2018). Efficient Blue and White Perovskite Light-Emitting Diodes via Manganese Doping. Joule *2*, 2421–2433. https://doi.org/10.1016/j.joule.2018.08.005.
22. Liu, M., Jiang, N., Huang, H., Lin, J., Huang, F., Zheng, Y., and Chen, D. (2021). Ni2+-Doped CsPbI3 Perovskite Nanocrystals with near-Unity Photoluminescence Quantum Yield and Superior Structure Stability for Red Light-Emitting Devices. Chem. Eng. J. *413*, 127547. https://doi.org/10.1016/j.cej.2020.127547.
23. Shen, W., Zhang, J., Dong, R., Chen, Y., Yang, L., Chen, S., Su, Z., Dai, Y., Cao, K., Liu, L., et al. (2021). Stable and Efficient Red Perovskite Light-Emitting Diodes Based on Ca2+-Doped CsPbI3 Nanocrystals. Research *2021*, 9829374. https://doi.org/10.34133/2021/9829374.
24. Lu, M., Zhang, X., Zhang, Y., Guo, J., Shen, X., Yu, W.W., and Rogach, A.L. (2018). Simultaneous Strontium Doping and Chlorine Surface Passivation Improve Luminescence Intensity and Stability of CsPbI3 Nanocrystals Enabling Efficient Light-Emitting Devices. Adv. Mater. *30*, 1804691. https://doi.org/10.1002/adma.201804691.
25. Vashishtha, P., Griffith, B.E., Brown, A.A., Hooper, T.J., Fang, Y., Ansari, M.S., Bruno, A., Pu, S.H., Mhaisalkar, S.G., White, T., and Hanna, J.V. (2020). Performance Enhanced Light-Emitting Diodes Fabricated from

Nanocrystalline CsPbBr3 with In Situ Zn2+ Addition. ACS Appl. Electron. Mater. *2*, 4002–4011. https://doi.org/10.1021/acsaelm.0c00827.

26. Cai, X.-Y., Yu, Y., Ye, Y.-C., Shen, Y., Guo, M.-L., Wang, J.-K., Shen, K.-C., Li, Y.-Q., and Tang, J.-X. (2021). Improving the Efficiency and Stability of Inorganic Red Perovskite Light-Emitting Diodes Using Traces of Zinc Ions. J. Mater. Chem. C *9*, 16682–16692. https://doi.org/10.1039/D1TC03846J.
27. Shen, X., Zhang, Y., Kershaw, S.V., Li, T., Wang, C., Zhang, X., Wang, W., Li, D., Wang, Y., Lu, M., et al. (2019). Zn-Alloyed CsPbI3 Nanocrystals for Highly Efficient Perovskite Light-Emitting Devices. Nano Lett. *19*, 1552–1559. https://doi.org/10.1021/acs.nanolett.8b04339.
28. Ahmed, G.H., Liu, Y., Bravić, I., Ng, X., Heckelmann, I., Narayanan, P., Fernández, M.S., Monserrat, B., Congreve, D.N., and Feldmann, S. (2022). Luminescence Enhancement Due to Symmetry Breaking in Doped Halide Perovskite Nanocrystals. J. Am. Chem. Soc. *144*, 15862–15870. https://doi.org/10.1021/jacs.2c07111.
29. Futscher, M.H., Gangishetty, M.K., Congreve, D.N., and Ehrler, B. (2020). Manganese Doping Stabilizes Perovskite Light-Emitting Diodes by Reducing Ion Migration. ACS Appl. Electron. Mater. *2*, 1522–1528. https://doi.org/10.1021/acsaelm.0c00125.
30. Xu, Y., Wang, H., Chen, Y., Chen, L., and Xie, Z. (2022). Efficient Sky-Blue Light-Emitting Diodes Based on Oriented Perovskite Nanoplates. Adv. Opt. Mater. *10* (*1*), 2101525. https://doi.org/10.1002/adom.202101525.
31. Chen, X., Huang, J., Gao, F., and Xu, B. (2023). Phosphine Oxide Additives for Perovskite Light-Emitting Diodes and Solar Cells. Chem *9*, 562–575. https://doi.org/10.1016/j.chempr.2023.01.002.
32. Dong, Q., Lei, L., Mendes, J., and So, F. (2020). Operational Stability of Perovskite Light Emitting Diodes. J. Phys. Mater. *3*, 012002. https://doi.org/10.1088/2515-7639/ab60c4.
33. Zou, C., Liu, Y., Ginger, D.S., and Lin, L.Y. (2020). Suppressing Efficiency Roll-Off at High Current Densities for Ultra-Bright Green Perovskite Light-Emitting Diodes. ACS Nano *14*, 6076–6086. https://doi.org/10.1021/acsnano.0c01817.
34. Zeng, J., Qi, Y., Liu, Y., Chen, D., Ye, Z., and Jin, Y. (2022). ZnO-Based Electron-Transporting Layers for Perovskite Light-Emitting Diodes: Controlling the Interfacial Reactions. J. Phys. Chem. Lett. *13*, 694–703. https://doi.org/10.1021/acs.jpclett.1c04117.
35. Veeramuthu, L., Liang, F.-C., Zhang, Z.-X., Cho, C.-J., Ercan, E., Chueh, C.-C., Chen, W.-C., Borsali, R., and Kuo, C.-C. (2020). Improving the Performance and Stability of Perovskite Light-Emitting Diodes by a Polymeric Nanothick Interlayer-Assisted Grain Control Process. ACS Omega *5*, 8972–8981. https://doi.org/10.1021/acsomega.0c00758.
36. Li, N., Jia, Y., Guo, Y., and Zhao, N. (2022). Ion Migration in Perovskite Light-Emitting Diodes: Mechanism, Characterizations, and Material and Device Engineering. Adv. Mater. *34*, 2108102. https://doi.org/10.1002/adma.202108102.
37. Cheng, T., Tumen-Ulzii, G., Klotz, D., Watanabe, S., Matsushima, T., and Adachi, C. (2020). Ion Migration-Induced Degradation and Efficiency Roll-off in Quasi-2D Perovskite Light-Emitting Diodes. ACS Appl. Mater. Interfaces *12*, 33004–33013. https://doi.org/10.1021/acsami.0c06737.
38. Dong, Q., Mendes, J., Lei, L., Seyitliyev, D., Zhu, L., He, S., Gundogdu, K., and So, F. (2020). Understanding the Role of Ion Migration in the Operation of Perovskite Light-Emitting Diodes by Transient Measurements. ACS Appl. Mater. Interfaces *12*, 48845–48853. https://doi.org/10.1021/acsami.0c14269.
39. Gunnarsson, W.B., Xu, Z., Noel, N.K., and Rand, B.P. (2022). Improved Charge Balance in Green Perovskite Light-Emitting Diodes with Atomic-Layer-Deposited Al2O3. ACS Appl. Mater. Interfaces *14*, 34247–34252. https://doi.org/10.1021/acsami.2c00860.
40. Zou, Y., Ban, M., Yang, Y., Bai, S., Wu, C., Han, Y., Wu, T., Tan, Y., Huang, Q., Gao, X., et al. (2018). Boosting Perovskite Light-Emitting Diode Performance via Tailoring Interfacial Contact. ACS Appl. Mater. Interfaces *10*, 24320–24326. https://doi.org/10.1021/acsami.8b07438.
41. Wang, H., Gong, X., Zhao, D., Zhao, Y.-B., Wang, S., Zhang, J., Kong, L., Wei, B., Quintero-Bermudez, R., Voznyy, O., et al. (2020). A Multi-Functional Molecular Modifier Enabling Efficient Large-Area Perovskite Light-Emitting Diodes. Joule *4*, 1977–1987. https://doi.org/10.1016/j.joule.2020.07.002.
42. Dong, Y., Wang, Y.-K., Yuan, F., Johnston, A., Liu, Y., Ma, D., Choi, M.-J., Chen, B., Chekini, M., Baek, S.-W., et al. (2020). Bipolar-Shell Resurfacing for Blue LEDs Based on Strongly Confined Perovskite Quantum Dots. Nat. Nanotechnol. *15*, 668–674. https://doi.org/10.1038/s41565-020-0714-5.
43. Sun, C., Jiang, Y., Cui, M., Qiao, L., Wei, J., Huang, Y., Zhang, L., He, T., Li, S., Hsu, H.-Y., et al. (2021). High-Performance Large-Area Quasi-2D Perovskite Light-Emitting Diodes. Nat. Commun. *12*, 2207. https://doi.org/10.1038/s41467-021-22529-x.
44. Jiang, Y., Cui, M., Li, S., Sun, C., Huang, Y., Wei, J., Zhang, L., Lv, M., Qin, C., Liu, Y., and Yuan, M. (2021). Reducing the Impact of Auger Recombination in Quasi-2D Perovskite Light-Emitting Diodes. Nat. Commun. *12*, 336. https://doi.org/10.1038/s41467-020-20555-9.
45. Matsushima, T., Bencheikh, F., Komino, T., Leyden, M.R., Sandanayaka, A.S.D., Qin, C., and Adachi, C. (2019). High Performance from Extraordinarily Thick Organic Light-Emitting Diodes. Nature *572*, 502–506. https://doi.org/10.1038/s41586-019-1435-5.
46. DenBaars, S.P., Feezell, D., Kelchner, K., Pimputkar, S., Pan, C.-C., Yen, C.-C., Tanaka, S., Zhao, Y., Pfaff, N., Farrell, R., et al. (2013). Development of Gallium-Nitride-Based Light-Emitting Diodes (LEDs) and Laser Diodes for Energy-Efficient Lighting and Displays. Acta Mater. *61*, 945–951. https://doi.org/10.1016/j.actamat.2012.10.042.
47. Li, Z., Cao, K., Li, J., Du, X., Tang, Y., and Yu, B. (2020). Modification of Interface between PEDOT:PSS and Perovskite Film Inserting an Ultrathin LiF Layer for Enhancing Efficiency of Perovskite Light-Emitting Diodes. Org. Electron. *81*, 105675. https://doi.org/10.1016/j.orgel.2020.105675.
48. Yoon, E., Jang, K.Y., Park, J., and Lee, T.-W. (2021). Understanding the Synergistic Effect of Device Architecture Design toward Efficient Perovskite Light-Emitting Diodes Using Interfacial Layer Engineering. Adv. Mater. Interfac. *8*, 2001712. https://doi.org/10.1002/admi.202001712.
49. Zhao, H., Chen, H., Bai, S., Kuang, C., Luo, X., Teng, P., Yin, C., Zeng, P., Hou, L., Yang, Y., et al. (2021). High-Brightness Perovskite Light-Emitting Diodes Based on FAPbBr3 Nanocrystals with Rationally Designed Aromatic Ligands. ACS Energy Lett. *6*, 2395–2403. https://doi.org/10.1021/acsenergylett.1c00812.
50. Woo, S.-J., Kim, J.S., and Lee, T.-W. (2021). Characterization of Stability and Challenges to Improve Lifetime in Perovskite LEDs. Nat. Photonics *15*, 630–634. https://doi.org/10.1038/s41566-021-00863-2.
51. Warby, J.H., Wenger, B., Ramadan, A.J., Oliver, R.D.J., Sansom, H.C., Marshall, A.R., and Snaith, H.J. (2020). Revealing Factors Influencing the Operational Stability of Perovskite Light-Emitting Diodes. ACS Nano *14*, 8855–8865. https://doi.org/10.1021/acsnano.0c03516.
52. Shan, Q., Li, J., Song, J., Zou, Y., Xu, L., Xue, J., Dong, Y., Huo, C., Chen, J., Han, B., and Zeng, H. (2017). All-Inorganic Quantum-Dot Light-Emitting Diodes Based on Perovskite Emitters with Low Turn-on Voltage and High Humidity Stability. J. Mater. Chem. C *5*, 4565–4570. https://doi.org/10.1039/C6TC05578H.
53. Wu, Z., Jiang, M., Liu, Z., Jamshaid, A., Ono, L.K., and Qi, Y. (2020). Highly Efficient Perovskite Solar Cells Enabled by Multiple Ligand Passivation. Adv. Energy Mater. *10*, 1903696. https://doi.org/10.1002/aenm.201903696.
54. Péan, E.V., Dimitrov, S., De Castro, C.S., Davies, M.L., and Davies, L. (2020). Interpreting Time-Resolved Photoluminescence of Perovskite Materials. Phys. Chem. Chem. Phys. *22*, 28345–28358. https://doi.org/10.1039/D0CP04950F.
55. Lee, C.M., Choi, D.H., Islam, A., Kim, D.H., Kim, T.W., Jeong, G.-W., Cho, H.W., Park, M.J., Shah, S.H.U., Chae, H.J., et al. (2022). Improved Device Efficiency and Lifetime of Perovskite Light-Emitting Diodes by Size-Controlled Polyvinylpyrrolidone-Capped Gold Nanoparticles with Dipole Formation. Sci. Rep. *12*, 2300. https://doi.org/10.1038/s41598-022-05935-z.

56. Forrest, S.r., Bradley, D.d. c., and Thompson, M.e. (2003). Measuring the Efficiency of Organic Light-Emitting Devices. Adv. Mater. *15*, 1043–1048. https://doi.org/10.1002/adma.200302151.

57. de Mello, J.C., Wittmann, H.F., and Friend, R.H. (1997). An Improved Experimental Determination of External Photoluminescence Quantum Efficiency. Adv. Mater. *9*, 230–232. https://doi.org/10.1002/adma.19970090308.

58. Parrott, E.S., Milot, R.L., Stergiopoulos, T., Snaith, H.J., Johnston, M.B., and Herz, L.M. (2016). Effect of Structural Phase Transition on Charge-Carrier Lifetimes and Defects in CH3NH3SnI3 Perovskite. J. Phys. Chem. Lett. *7*, 1321–1326. https://doi.org/10.1021/acs.jpclett.6b00322.